Article

Antarctic ice dynamics amplified by Northern Hemisphere sea-level forcing

https://doi.org/10.1038/s41586-020-2916-2

Received: 20 September 2019

Accepted: 16 September 2020

Published online: 25 November 2020

Check for updates

Natalya Gomez[1]✉, Michael E. Weber[2], Peter U. Clark[3,4], Jerry X. Mitrovica[5] & Holly K. Han[1]

Sea-level rise due to ice loss in the Northern Hemisphere in response to insolation and greenhouse gas forcing is thought to have caused grounding-line retreat of marine-based sectors of the Antarctic Ice Sheet (AIS)[1–3]. Such interhemispheric sea-level forcing may explain the synchronous evolution of global ice sheets over ice-age cycles. Recent studies that indicate that the AIS experienced substantial millennial-scale variability during and after the last deglaciation[4–7] (roughly 20,000 to 9,000 years ago) provide further evidence of this sea-level forcing. However, global sea-level change as a result of mass loss from ice sheets is strongly nonuniform, owing to gravitational, deformational and Earth rotational effects[8], suggesting that the response of AIS grounding lines to Northern Hemisphere sea-level forcing is more complicated than previously modelled[1,2,6]. Here, using an ice-sheet model coupled to a global sea-level model, we show that AIS dynamics are amplified by Northern Hemisphere sea-level forcing. As a result of this interhemispheric interaction, a large or rapid Northern Hemisphere sea-level forcing enhances grounding-line advance and associated mass gain of the AIS during glaciation, and grounding-line retreat and mass loss during deglaciation. Relative to models without these interactions, the inclusion of Northern Hemisphere sea-level forcing in our model increases the volume of the AIS during the Last Glacial Maximum (about 26,000 to 20,000 years ago), triggers an earlier retreat of the grounding line and leads to millennial-scale variability throughout the last deglaciation. These findings are consistent with geologic reconstructions of the extent of the AIS during the Last Glacial Maximum and subsequent ice-sheet retreat, and with relative sea-level change in Antarctica[3–7,9,10].

There are several mechanisms to explain near-synchronous interhemispheric climate changes on orbital timescales despite opposite insolation forcing[11,12]. However, synchronous changes in surface climate cannot explain synchronous changes in the Northern Hemisphere and Antarctic ice sheets[3,13], because such changes would have induced opposing ice-sheet surface-mass-balance responses, with warming climate over the AIS leading to a more positive surface mass balance[3]. In the absence of surface melting, mechanisms that affect the primary controls on AIS mass balance (basal melting of buttressing ice shelves and ice discharge across grounding lines of marine-based sectors) are therefore required for ice-sheet synchronization.

Studies have shown that an increase in subsurface warming from changes in ocean circulation contributes to AIS deglaciation[4,5,14,15]. Marine-based sectors of ice sheets are also vulnerable to sea-level change at their grounding lines: A local fall in sea level may slow or stabilize grounding-line retreat, or initiate or enhance grounding-line advance, whereas a rise in sea level may slow grounding-line advance, or initiate or enhance grounding-line retreat[16,17].

Previous work suggests that sea-level rise from deglaciation of Northern Hemisphere ice sheets triggered the retreat of the grounding lines of the AIS and thus synchronized ice-sheet variability globally[1,2,18,19]. Well-dated geologic records of AIS fluctuations support synchronization on orbital timescales[3,13] and identify links between periods of sea-level rise and millennial-scale AIS variability during the last deglaciation (20,000–9,000 years ago; 20–9 ka). For example, deep-sea sediments from Scotia Sea's Iceberg Alley record eight discrete episodes of increased flux of iceberg-rafted debris originating from the AIS during the last deglaciation[4]. Three of these AIS discharge (AID) events occurred at the same time as well-documented periods of sea-level rise, suggesting a possible link: AID7 corresponds to the onset of deglacial sea-level rise about 19.5–19 ka[3,20], AID6 corresponds to Meltwater Pulse 1A (MWP-1A) around 14.5 ka[21], and AID2 corresponds to an acceleration of sea-level rise during the early Holocene, starting roughly 11.5 ka[22,23]. Additional evidence for this dynamic ice-sheet behaviour comes from isotopic records from a horizontal ice core in the Patriot Hills of the Weddell Sea Embayment[6], which suggest that the ice surface in that region lowered by at least 600 m during AID6 and around AID2. Finally, marine records from the Ross Sea indicate a step-wise retreat of the grounding line of the West Antarctic Ice Sheet, coincident with AID events 6 and 2 (ref. [7]). The iceberg-rafted debris record since AID1 (about 10.4–9 ka)

[1]Department of Earth and Planetary Sciences, McGill University, Montreal, Quebec, Canada. [2]Department of Geochemistry and Petrology, Institute for Geosciences, University of Bonn, Bonn, Germany. [3]College of Earth, Ocean, and Atmospheric Sciences, Oregon State University, Corvallis, OR, USA. [4]School of Geography and Environmental Sciences, University of Ulster, Coleraine, UK. [5]Department of Earth and Planetary Sciences, Harvard University, Cambridge, MA, USA. ✉e-mail: natalya.gomez@mcgill.ca

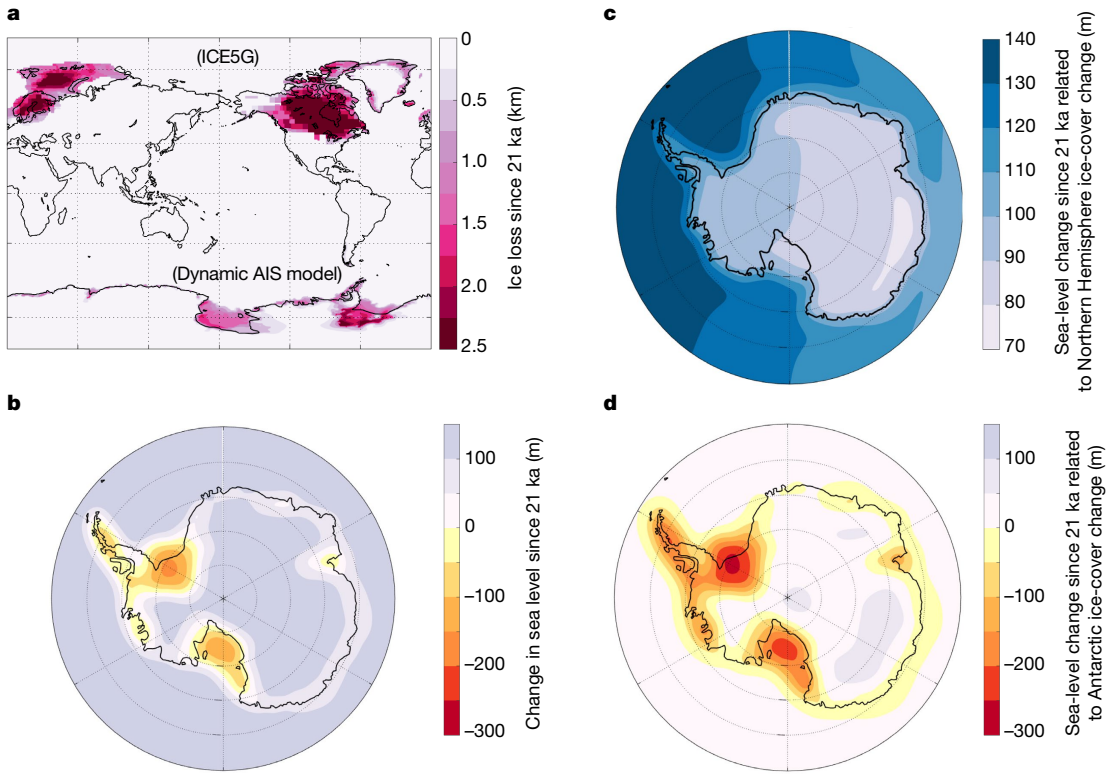

Fig. 1 | Contributions to deglacial sea-level changes in Antarctica. a, Changes in grounded ice thickness since 21 ka in the coupled ice-sheet–sea-level simulation, based on the ICE5G[27] ice history in the Northern Hemisphere and the dynamic ice-sheet model in Antarctica. **b**, Predicted total relative sea-level change since 21 ka in Antarctica. **c**, Component of sea-level change in **b** associated with ice-cover changes in the Northern Hemisphere in the ICE5G[27] ice history, computed from a simulation with only the sea-level model. **d**, Difference between **b** and **c**, showing changes in relative sea level associated with Antarctic ice-cover changes.

suggests that there has been a substantial reduction in the amplitude of iceberg-flux variability over the past 8 kyr[24] and global-mean sea level has experienced only decimetre-scale changes over the past 6 kyr[25]. Current uncertainties in these far-field sea-level reconstructions and in the age model for Antarctic iceberg-rafted debris cores[4] preclude determination of the relative phasing between the AID events and the sea-level change associated with Northern Hemisphere ice melting, but modelling can provide insights into the mechanisms that led to these observed changes.

Here we investigate possible interhemispheric ice-sheet coupling through sea-level change over the past 40,000 years and assess its effect on the evolution and behaviour of the AIS. We model the evolution

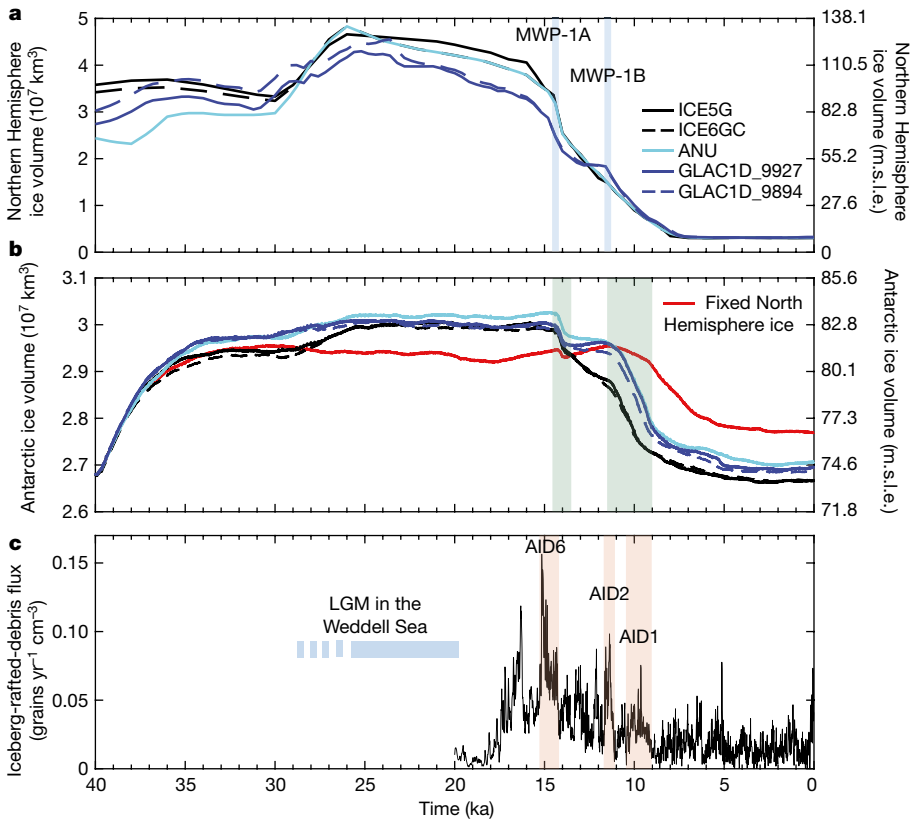

Fig. 2 | Timing of Northern Hemisphere sea-level forcing and its influence on Antarctic ice volume changes. a, Prescribed changes in Northern Hemisphere ice volume from the ICE5G[27] (solid black line), ICE6GC[31] (dashed black line) and ANU[30] (solid cyan line) ice histories. Two composite ice histories, in which ice cover over North America and Greenland in ICE5G has been replaced by GLAC1D[29] regional ice histories (blue solid and dashed lines), are also shown. Blue vertical bands indicate the timings of MWP-1A[21] and MWP-1B[22]. **b**, Changes in Antarctic ice volume predicted in simulations with fixed (red line) and evolving (blue, cyan and black lines; ice histories as in **a**) Northern Hemisphere ice. Green vertical bands indicate periods during MWP-1A and the early Holocene in the model simulations that are examined in the text and other figures. **c**, Iceberg-rafted-debris flux from sediment cores in Iceberg Alley[4] (Methods, Extended Data Fig. 9). Vertical red bands indicate the timing of AID events 1, 2 and 6; horizontal blue bands indicate the extent of the LGM in the Weddell Sea[3]. m.s.l.e. indicates metres sea-level equivalent.

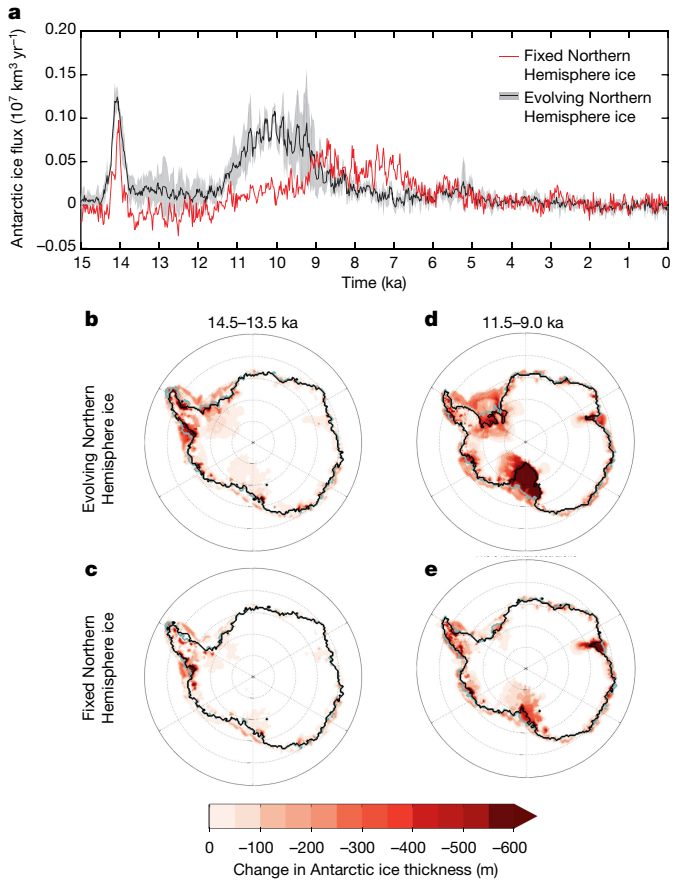

Fig. 3 | Enhanced Antarctic ice loss during MWP-1A and the early Holocene. **a**, Rate of change of Antarctic ice volume, including grounded and floating ice, calculated as a 100-year running mean, predicted from simulations including (black line) and excluding (red line) Northern Hemisphere ice-cover changes. The black line and shading represent the mean and standard deviation of predictions generated with the five ice histories described in the text. **b**–**e**, Change in Antarctic ice thickness during MWP-1A (14.5–13.5 ka; **b**, **c**) and during the early Holocene, starting from the time of MWP-1B (11.5–9 ka; **d**, **e**). Panels **b** and **d** are based on simulations that include ice-mass flux from the Northern Hemisphere from the ICE5G ice history. These simulations predict Antarctic ice loss equivalent to global-mean sea-level rise of 1.14 m and 1.95 m for MWP-1A (**b**) and the early Holocene (**d**), respectively. Panels **c** and **e** are based on simulations in which Northern Hemisphere ice sheets remain fixed throughout the simulation. The grey–blue and black lines indicate the grounding-line position at the start and end of the time interval, respectively.

of the AIS and global sea-level changes using the Pennsylvania State University three-dimensional ice-sheet model coupled to a gravitationally self-consistent global sea-level model that includes viscoelastic deformation of the solid Earth, rotational feedbacks and migrating shorelines[26] (see Methods).

Deglacial sea-level change in Antarctica

Figure 1a shows ice loss since 21 ka from the AIS, as calculated in a coupled ice-sheet–sea-level model simulation, and from Northern Hemisphere ice sheets, derived from the ICE5G ice history[27]. The AIS simulation is based on parameters identified in a large ensemble analysis as best fitting a range of palaeo and modern data constraints[28], and is characterized by a global-mean sea-level-equivalent mass loss of 5 m from the AIS, with 107 m from the Northern Hemisphere in ICE5G (see Methods and Extended Data Fig. 1 for results of simulations with a larger AIS contribution to global-mean sea level). Peak sea-level fall is predicted to reach 150 m in previously glaciated regions in Antarctica, while the bedrock deepens in the interior of Antarctica and sea level rises by 150 m in the surrounding ocean (Fig. 1b). Mass loss from Northern Hemisphere ice sheets contributes a sea-level rise that increases from 80 m in East Antarctica to 130 m in West Antarctica (Fig. 1c), in agreement with previous work[3]. This sea-level gradient is driven by a shift of the Earth's rotation axis towards North America in the Northern Hemisphere, where most ice is being lost (Fig. 1a), and towards East Antarctica in the Southern Hemisphere, driving lower-than-average sea-level rise in these regions and higher-than-average sea-level rise in the opposing quadrants of the Earth's surface (which include West Antarctica and Eurasia). By contrast, mass loss from the AIS drives a sea-level fall of up to 300 m in previously glaciated regions of Antarctica, owing to gravitationally driven lowering of the sea surface and viscoelastic uplift of the solid Earth under the areas of ice mass loss (Fig. 1d). The sea-level fall associated with local AIS loss thus dominates the total Antarctic signal in these areas. However, sea-level rise due to the much larger Northern Hemisphere ice-mass loss substantially decreases the geographic spread and magnitude of sea-level fall at Antarctic grounding lines over the last deglaciation (compare Figs. 1b and d).

AIS response to Northern Hemisphere sea-level forcing

We quantify how sea-level changes associated with Northern Hemisphere ice-sheet variations (Figs. 1c, 2a) influenced the dynamics of the AIS leading up to the Last Glacial Maximum (LGM; around 26–20 ka[13]) and during the last deglaciation. We compare AIS mass changes predicted from: (1) model simulations that include the evolution of the Northern Hemisphere ice sheets prescribed from five ice-history reconstructions[27,29–31]; and (2) a simulation in which the Northern Hemisphere ice sheets remain fixed in their initial configuration at 40 ka and do not contribute to sea-level changes in Antarctica over the simulation (Fig. 2b, Extended Data Fig. 8, Methods). In the simulations, Northern Hemisphere ice growth leading up to the LGM contributes a sea-level fall beginning around 30 ka (Fig. 2a), which drives additional AIS growth at about 28 ka (Fig. 2b). This growth occurs primarily in the Antarctic Peninsula and Weddell Sea regions (Extended Data Figs. 2c, 3, at 20 ka; Extended Data Fig. 4), and is consistent with evidence for when ice reached its LGM extent in these regions[3].

During the last deglaciation, sea-level rise from Northern Hemisphere ice-sheet retreat (Fig. 2a) greatly enhances the magnitude and rate of AIS mass loss since 15 ka (Fig. 2b, Extended Data Figs. 2, 3). By contrast, the simulation with no Northern Hemisphere sea-level forcing is characterized by net AIS growth over much of the same period (Fig. 2b). In particular, with fixed Northern Hemisphere ice, extensive grounded ice remains in the Weddell Sea and, to a lesser extent, the Ross Sea regions until the present day (Extended Data Figs. 2, 3), whereas including a Northern Hemisphere sea-level forcing causes these regions to completely deglaciate, reaching a modern Antarctic ice volume close to the observed volume (2.69×10^7 km^3; ref. [32]). Differences in AIS evolution are greatest in the Weddell Sea region (Extended Data Fig. 4), where the largest sea-level forcing is predicted from Northern Hemisphere ice-mass loss (Fig. 1c). We have highlighted the sensitivity of the ice sheet to this geographic variability in Extended Data Fig. 7.

MWP-1A and early Holocene ice loss

Our simulations suggest that an increase in AIS mass loss since 15 ka, driven by Northern Hemisphere sea-level forcing, contributed to MWP-1A (around 14.5 ka) and support an Antarctic source for early-Holocene acceleration in sea-level rise[33] (Fig. 2). Specifically, the AIS simulations that include a Northern Hemisphere sea-level forcing during the deglaciation show distinct corresponding periods of rapid mass loss (Figs. 2b, 3a) during and after these two episodes of rapid sea-level rise. This behaviour may therefore explain the large

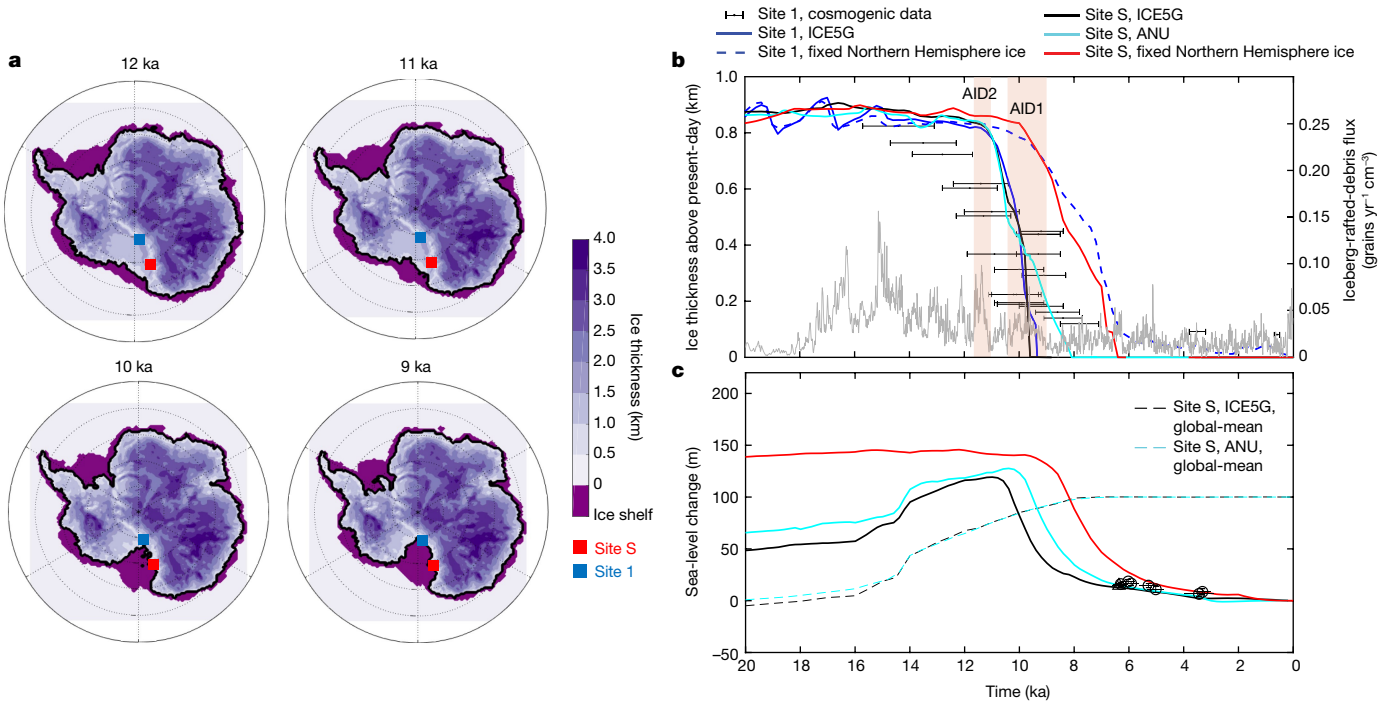

Fig. 4 | Agreement of predicted sea-level and ice-cover changes with geological records in the Ross Sea sector. a, Predicted Antarctic ice cover in the simulation that includes Northern Hemisphere ice from ICE5G[27] at snapshots in time as the Ross Sea region deglaciates. **b**, Predicted ice thickness (left axis) above the present-day thickness at site S (red squares in **a**) and site 1 (blue squares in **a**; ref. [35]), for simulations in which Northern Hemisphere ice cover is evolving according to ICE5G[27] or ANU[30] ice histories (black and cyan lines for site S, solid blue line for site 1) or fixed (red line for site S, dashed blue line for site 1). Error bars show cosmogenic exposure age data with 2σ uncertainty from ref. [35] at site 1. The grey time series is the recorded flux of Antarctic iceberg-rafted debris from Fig. 2c (right axis); red vertical bands indicate AID events 1 and 2. **c**, Predictions of relative sea-level change at site S for evolving (solid black and cyan lines) and fixed (solid red line) Northern Hemisphere ice cover. Dashed black and cyan lines indicate the contribution to global-mean sea-level change from Northern Hemisphere ice-cover prescribed in ICE5G[27] and ANU[30] ice histories, respectively. Black markers with 2σ error bars show two-way (circles) or lower-bound (triangles) relative sea-level constraints[9].

increases in iceberg-rafted-debris flux in Iceberg Alley (AID events 6, 2 and 1; ref. [4]; Fig. 2c) and mass loss from the Weddell Sea[6] and Ross Sea[7] regions at these times. Alternative physical processes (such as ocean and atmospheric forcing) must be sought to explain the other AIS discharge events during the last deglaciation[4].

In the case of MWP-1A, the AIS experiences more extensive mass loss (Figs. 2b, 3a, Extended Data Fig. 5) in the simulations in which Northern Hemisphere ice sheets evolve than in the simulation in which they are fixed and AIS mass loss is driven only by climate forcing on the ice sheet[14] (Fig. 3a–c). The net volume of ice lost in the latter simulation over this period is 2.5–3 times less than predicted in the former across the range of evolving Northern Hemisphere ice histories we consider. In the case of the early Holocene, including Northern Hemisphere sea-level forcing increases the rate of AIS mass loss by up to a factor of about 4, starting around 11.5 ka (Fig. 3a)—the time of MWP-1B suggested by the far-field Barbados sea-level record[23] and AID2 (ref. [4]). This mass loss continues throughout AID1 until 9.5–9 ka (Figs. 2, 3, Extended data Fig. 5), with substantial grounding-line retreat in the Ross Sea and Weddell Sea regions (compare Fig. 3d and Fig. 3e). The amplified AIS response during the early Holocene occurs regardless of whether there is an acceleration in Northern Hemisphere ice loss during that time (compare Extended Data Fig. 5a with ICE5G[27] and Extended Data Fig. 5b, c with ICE6G[31] and ANU[30]). It is also consistent with the hypothesis of a substantial or dominant Antarctic source for acceleration in global-mean sea-level rise[31,33] during this period (Extended Data Fig. 6).

We have confirmed that the general behaviour evident in Figs. 2 and 3 holds for coupled model simulations using a range of Earth and ice-model parameters (Extended Data Figs. 1, 8). The largest difference is found in simulations with less basal sliding. These simulations result in a larger LGM ice sheet (Extended Data Fig. 1), with AIS growth in the first half of the simulations being less sensitive to Northern Hemisphere ice growth and the associated sea-level fall than simulations with more basal sliding. The concordance between the two simulations with less basal sliding is probably because the AIS margin nearly reaches its maximum possible extent at the continental shelf edge in both cases.

Comparison to geologic records

We next consider local ice-sheet and sea-level changes in the Ross Sea region where there are reconstructions of relative sea level[9,34] (Southern Scott Coast; site S in Fig. 4a), grounding-line migration[7] and changes in ice-surface elevation (site 1 in Fig. 4; other sites in the Ross Sea and Weddell Sea regions are shown in Extended Data Figs. 10, 11)[35] that provide a test of the local response to Northern Hemisphere sea-level forcing. When this forcing is included, deglaciation of the region is predicted to begin in the early Holocene (Fig. 4a), with regional ice thinning occurring from 11 ka to 8 ka (blue, black and cyan curves show thinning at sites S and 1 in Fig. 4b). This model result is consistent with observations of ice-surface lowering at site 1 (ref. [35]; Fig. 4b, error bars; nearby sites 3–5, which are just outside the region of substantial ice thinning, are discussed in Extended Data Fig. 11), a grounding-line retreat of at least 200 km in the Ross Sea[7] and a peak iceberg-rafted-debris flux during AID events 2 and 1 (ref. [4]). By contrast, this retreat takes place from 10 ka to 6 ka at sites S and 1 when Northern Hemisphere sea-level forcing is not included in the simulation (Fig. 4b), which is inconsistent with a relatively low observed iceberg-rafted-debris flux since about 8.5 ka[24] (Fig. 4b, grey line).

At site S, local sea-level change during the deglacial phase is initially dominated by Northern-Hemisphere-driven sea-level rise. However, as local ice loss begins (about 11 ka), the associated gravitational and

deformational effects dominate the local sea-level change (Fig. 4c). When the Northern-Hemisphere-driven sea-level forcing is excluded (Fig. 4c), relative sea-level fall is predicted to begin later (around 9 ka), coincident with local ice loss for this simulation (Fig. 4b); there is almost no change in relative sea level before 10 ka. The oldest relative sea-level indicators from this area (about 6.5 ka; Fig. 4c) are more consistent with the lower relative sea level predicted by the simulations that include Northern Hemisphere sea-level forcing. However, older indicators are needed to clearly corroborate this, especially given the uncertainty in the local viscoelastic structure of the Earth in this region.

Summary

We conclude that geographically variable sea-level changes around Antarctica, driven by Northern Hemisphere ice-sheet changes, strongly modulated the growth and decay of the AIS. Northern Hemisphere ice growth leading up to the LGM causes local sea-level fall and further AIS growth in our simulations, yielding a higher peak AIS volume at the LGM than without this forcing. Conversely, in our model, Northern Hemisphere ice loss during the last deglaciation produces a sea-level rise of 80–130 m in Antarctica, which drives earlier, greater and more rapid AIS retreat that is in better agreement with geologic evidence than predictions that omit this forcing. The simulations indicate that the Weddell Sea region of the AIS was subject to the largest sea-level changes driven by Northern Hemisphere ice changes, suggesting that ice-mass changes in this region were particularly sensitive to this far-field sea-level forcing. Finally, simulations with Northern Hemisphere sea-level forcing predict increases in AIS mass flux during MWP-1A and the early Holocene, consistent with multiple lines of geologic evidence for AIS mass loss at these times.

Online content

Any methods, additional references, Nature Research reporting summaries, source data, extended data, supplementary information, acknowledgements, peer review information; details of author contributions and competing interests; and statements of data and code availability are available at https://doi.org/10.1038/s41586-020-2916-2.

1. Denton, G. H. & Hughes, T. J. Milankovitch theory of ice ages: hypothesis of ice-sheet linkage between regional insolation and global climate. *Quat. Res.* **20**, 125–144 (1983).
2. Huybrechts, P. J. Sea-level changes at the LGM from ice-dynamic reconstructions of the Greenland and Antarctic ice sheets during the glacial cycles. *Quat. Sci. Rev.* **21**, 203–231 (2002).
3. Weber, M. E. et al. Interhemispheric ice-sheet synchronicity during the Last Glacial Maximum. *Science* **334**, 1265–1269 (2011).
4. Weber, M. E. et al. Millennial-scale variability in Antarctic ice-sheet discharge during the last deglaciation. *Nature* **510**, 134–138 (2014).
5. Golledge, N. R. et al. Antarctic contribution to meltwater pulse 1A from reduced Southern Ocean overturning. *Nat. Commun.* **5**, 5107 (2014).
6. Fogwill, C. J. et al. Antarctic ice sheet discharge driven by atmosphere–ocean feedbacks at the Last Glacial Termination. *Sci. Rep.* **7**, 39979 (2017).
7. Bart, P. J., DeCesare, M., Rosenheim, B. E., Majewski, W. & McGlannan, A. A centuries-long delay between a paleo-ice-shelf collapse and grounding-line retreat in the Whales Deep Basin, eastern Ross Sea, Antarctica. *Sci. Rep.* **8**, 12392 (2018).
8. Milne, G. A. & Mitrovica, J. X. Searching for eustasy in deglacial sea-level histories. *Quat. Sci. Rev.* **27**, 2292–2302 (2008).
9. Hall, B. L. & Denton, G. H. New relative sea-level curves for the southern Scott Coast, Antarctica: evidence for Holocene deglaciation of the western Ross Sea. *J. Quat. Sci.* **14**, 641–650 (1999).
10. Fogwill, C. J. et al. Southern Ocean carbon sink enhanced by sea-ice feedbacks at the Antarctic Cold Reversal. *Nat. Geosci.* **13**, 489–497 (2020).
11. Kawamura, K. et al. Northern Hemisphere forcing of climatic cycles in Antarctica over the past 360,000 years. *Nature* **448**, 912–916 (2007).
12. Huybers, P. & Denton, G. Antarctic temperature at orbital timescales controlled by local summer duration. *Nat. Geosci.* **1**, 787–792 (2008).
13. Clark, P. U. et al. The last glacial maximum. *Science* **325**, 710–714 (2009).
14. Pollard, D., Chang, W., Haran, M., Applegate, P. & DeConto, R. Large ensemble modeling of the last deglacial retreat of the West Antarctic Ice Sheet: comparison of simple and advanced statistical techniques. *Geosci. Model Dev.* **9**, 1697–1723 (2016).
15. Clark, P. U. et al. Oceanic forcing of penultimate deglacial and last interglacial sea-level rise. *Nature* **577**, 660–664 (2020).
16. Weertman, J. Stability of the junction of an ice sheet and an ice shelf. *J. Glaciol.* **13**, 3–11 (1974).
17. Schoof, C. Ice sheet grounding line dynamics: steady states, stability, and hysteresis. *J. Geophys. Res.* **112**, F03S28 (2007).
18. Denton, G. H., Hughes, T. J. & Karlén, W. Global ice-sheet system interlocked by sea level. *Quat. Res.* **26**, 3–26 (1986).
19. Tigchelaar, M., Timmermann, A., Friedrich, T., Heinemann, M. & Pollard, D. Nonlinear response of the Antarctic Ice Sheet to late Quaternary sea level and climate forcing. *Cryosphere* **13**, 2615–2631 (2019).
20. Yokoyama, Y., Lambeck, K., De Deckker, P., Johnston, P. & Fifield, L. K. Timing of the Last Glacial Maximum from observed sea-level minima. *Nature* **406**, 713–716 (2000); corrigendum **412**, 99 (2001).
21. Deschamps, P. et al. Ice-sheet collapse and sea-level rise at the Bølling warming 14,600 years ago. *Nature* **483**, 559–564 (2012).
22. Bard, E., Hamelin, B. & Delanghe-Sabatier, D. Deglacial meltwater pulse 1B and Younger Dryas sea levels revisited with boreholes at Tahiti. *Science* **327**, 1235–1237 (2010).
23. Abdul, N. A., Mortlock, R. A., Wright, J. D. & Fairbanks, R. G. Younger Dryas sea level and meltwater pulse 1B recorded in Barbados reef crest coral Acropora palmata. *Paleoceanography* **31**, 330–344 (2016).
24. Bakker, P., Clark, P. U., Golledge, N. R., Schmittner, A. & Weber, M. E. Centennial-scale Holocene climate variations amplified by Antarctic Ice Sheet discharge. *Nature* **541**, 72–76 (2017).
25. Hallmann, N. et al. Ice volume and climate changes from a 6000 year sea-level record in French Polynesia. *Nat. Commun.* **9**, 285 (2018).
26. Gomez, N., Pollard, D. & Mitrovica, J. X. A 3-D coupled ice sheet – sea level model applied to Antarctica through the last 40 ky. *Earth Planet. Sci. Lett.* **384**, 88–99 (2013).
27. Peltier, W. R. Global glacial isostasy and the surface of the ice-age Earth: the ICE-5G (VM2) model and GRACE. *Annu. Rev. Earth Planet. Sci.* **32**, 111–149 (2004).
28. Pollard, D., Gomez, N. & DeConto, R. M. Variations of the Antarctic Ice Sheet in a coupled ice sheet-Earth-sea level model: sensitivity to viscoelastic Earth properties. *J. Geophys. Res. Earth Surf.* **122**, 2124–2138 (2017).
29. Tarasov, L., Dyke, A. S., Neal, R. M. & Peltier, W. R. A data-calibrated distribution of deglacial chronologies for the North American ice complex from glaciological modeling. *Earth Planet. Sci. Lett.* **315–316**, 30–40 (2012).
30. Lambeck, K., Rouby, H., Purcell, A., Sun, Y. & Sambridge, M. Sea level and global ice volumes from the Last Glacial Maximum to the Holocene. *Proc. Natl Acad. Sci. USA* **111**, 15296–15303 (2014).
31. Peltier, W. R., Argus, D. F. & Drummond, R. Space geodesy constrains ice age terminal deglaciation: the global ICE-6G_C (VM5a) model. *J. Geophys. Res. Solid Earth* **120**, 450–487 (2015).
32. Fretwell, P. et al. Bedmap2: improved ice bed, surface and thickness datasets for Antarctica. *Cryosphere* **7**, 375–393 (2013).
33. Bard, E., Hamelin, B., Deschamps, P. & Camoin, G. Comment on "Younger Dryas sea level and meltwater pulse 1B recorded in Barbados reefal crest coral *Acropora palmata*" by N. A. Abdul et al. *Paleoceanography* **31**, 1603–1608 (2016).
34. Briggs, R. D. & Tarasov, L. How to evaluate model-derived deglaciation chronologies: a case study using Antarctica. *Quat. Sci. Rev.* **63**, 109–127 (2013).
35. Jones, R., Whitehouse, P., Bentley, M., Small, D. & Dalton, A. Impact of glacial isostatic adjustment on cosmogenic surface-exposure dating. *Quat. Sci. Rev.* **212**, 206–212 (2019).

Methods

Coupled ice-sheet–sea-level modelling

The evolution of the AIS and global sea-level changes were modelled using the coupled ice-sheet–sea-level model developed and described in detail in ref. [26] and applied in refs. [28,36]. The model consists of the Pennsylvania State University (PSU) 3D ice-sheet model[37] coupled to a gravitationally self-consistent global sea-level model that includes viscoelastic deformation of the solid Earth, rotational feedbacks onto sea level and migrating shorelines[38,39].

PSU 3D is a finite-difference, ice-sheet–ice-shelf model that adopts hybrid combinations of the scaled shallow-ice and shallow-shelf equations[40,41] to treat ice dynamics, and includes grounding-line migration through a parameterization of flux across the grounding line[17]. This grounding-line treatment performs reasonably well in comparison with higher-order ice-sheet models[42] and facilitates the computational feasibility of glacial–interglacial timescale simulations. Basal sliding in the model is treated with a standard Weertman-type sliding law and basal sliding coefficients are determined through inverse fitting to ice thickness under regions with modern grounded ice[43]. In modern oceanic regions, where basal sliding is relatively unconstrained, the coefficient is set to 10^{-5} m yr^{-1} Pa^{-2} in simulations presented in the main text and to 10^{-6} m yr^{-1} Pa^{-2} in additional simulations summarized in Extended Data Fig. 1, representing the range identified[28] to best fit a suite of palaeo ice-sheet and sea-level constraints. Alternative basal sliding laws have been proposed[44,45], but model treatments remain unverified by observations and should be explored further in future work. Other ice model parameters such as the calving coefficient and ocean melt factor are similarly set to best-fitting values identified in refs. [14,28]. Here and in these references, atmospheric climate forcing was applied by perturbing modern climatology (ALBMAP[46]) to mimic past conditions according to a deep-sea δ^{18}O stack[47]. Sub-ice-shelf melt rates are determined through a parameterization that depends on subsurface oceanic temperatures from ref. [48], with sensitivity inferred from the aforementioned large ensemble model–data comparisons[28]. We note that the best-fitting simulations in these studies produce a relatively small contribution from Antarctica to sea level over the last deglaciation. We therefore explore simulations with a larger excess ice volume at the LGM and greater ice loss through the deglaciation in Extended Data Fig. 1.

Northern Hemisphere (NH) ice-cover variations were prescribed in the global sea-level model using five different ice histories: three global ice histories (ICE5G[27], ICE6GC[31] and the ANU model[30]) and two histories with GLAC1D reconstructions[29] over North America and Greenland and ICE5G elsewhere. These ice-history reconstructions are widely used, cover the whole time period under consideration and are constrained by glacial isostatic adjustment modelling and a suite of sea-level and ice-cover records.

The elastic and density structure of the solid Earth in the sea-level model are prescribed from the preliminary reference Earth model (PREM)[49]. Two different models of the viscosity structure of the Earth's mantle are adopted in the simulations. Figs. 1–4 show results using the 'LVZ' model, which is representative of structure beneath the West Antarctic. This model is characterized by a 50-km-thick lithosphere, a low-viscosity zone of 10^{19} Pa s extending from the base of the lithosphere to a depth of 200 km, and a viscosity of 2×10^{20} Pa s in the upper mantle and 3×10^{21} Pa s in the lower mantle. The LVZ model was adopted in refs. [28,36]. Additional simulations in Extended Data Fig. 1 adopt a viscosity structure that falls within a range of models that best fit a suite of global observations related to glacial isostatic adjustment[30,50]. The model, labelled 'HV', is characterized by a lithospheric thickness of 120 km and upper and lower mantle viscosities of 5×10^{20} Pa s and 5×10^{21} Pa s, respectively.

The ice-sheet model is run on a polar stereographic projection with a 20-km grid resolution, while sea-level calculations are performed up to spherical harmonic degree 512. To couple the models, the ice-sheet model first computes changes in Antarctic ice thickness over a 200-year 'coupling interval' (sensitivity tests described in ref. [26] show that this choice is sufficiently short for ice-age simulations). These AIS changes are then combined with NH ice cover—which is either fixed at its configuration at 40 ka throughout the run for 'fixed NH ice' simulations or evolves according to the chosen ice history in 'evolving NH ice' simulations (Extended Data Fig. 8)—over this interval. The combination is then used as input to the sea-level model to compute the associated global changes in sea level. The predicted changes in sea level, which are equivalent to the negative of changes in topography or bedrock elevation, are passed back to the ice-sheet model and used to update bedrock topography in Antarctica. The ice-sheet model then proceeds forward across another coupling interval and the process repeats over the full 40-kyr simulation. Initial conditions of the ice sheet at 40 ka are provided by a longer, full-glacial-cycle run of the ice-sheet model, along with bedrock deformation given by a simpler, elastic-lithosphere relaxed-asthenosphere (ELRA) model[51]. Global topography and bedrock elevation in Antarctica at the start of the simulation (40 ka) are initially unknown. They are determined through an iterative procedure, whereby the predicted modern topography at the end of a 40-kyr simulation is compared to observed topography (ETOPO2[52] globally and Bedmap2[32] in Antarctica), and the difference between the two is used to correct the initial topography at 40 ka in the next iteration. The process is repeated four times, which guarantees sufficient convergence of predicted and observed modern topography.

Iceberg Alley sites and iceberg-rafted debris (IBRD) record

Sample-based investigations have concentrated on deep-sea cores retrieved in the Scotia Sea's Iceberg Alley during *Marion Dufresne II* cruise 160 in March 2007. Sites MD07-3133 (57° 26′ S, 43° 27′ W; 3,101 m water depth; 32.8 m long) and MD07-3134 (59° 25′ S, 41° 28′ W; 3,663 m water depth; 58.2 m long) originate from the northern end of Dove Basin and Pirie Bank, respectively.

The age models of sites MD07-3133 and MD07-3134 are based on distinct dust–climate couplings between Southern Ocean sediment and the Antarctic EPICA Dronning Maud Land (EDML) ice core[53] on the EDML1 age model[54]. The EDML1 age model appears more consistent with local ash-layer correlations than the later AICC 2012 age model, which relies on interhemispheric methane correlation[55,56]. Comparison between age models (Extended Data Fig. 9c) shows older ages for the AICC 2012 age scale. Differences are minimal for the mid to late Holocene. At the time of MWP-1B, the difference is roughly 150 years, whereas it is 350 years during MWP-1A and about 500 years at the LGM. This means that for AIS discharge (AID) event 2 the shift is very small and the event aligns well with MWP-1B regardless of the age model. AID event 6 would extend from about 14.3 ka to 15.2 ka in AICC 2012, a range that still encompasses MWP-1A (14.65–14.3 ka), especially within the uncertainties of the ice-core age models, which increase from a few centuries for the time of MWP-1B up to a millennium for the LGM[55,56]. Therefore, the correlations we make here and the conclusions we draw hold regardless of the age model applied.

Magnetic susceptibility and Ca and Fe records measured through X-ray fluorescence can be used to study coherent and synchronous changes in dust deposition across much of the Southern Ocean and the AIS across the last deglaciation[4], and on longer, glacial–interglacial timescales[57,58]. IBRD counting was conducted every 1 cm on X-radiographs taken from 1-cm-thick slices cut out from the centre of each core segment and exposed to an X-ray system. The transitions from low to high and high to low IBRD contents form the basis of our AID event classification. The counting interval of 1 cm translates to 8–17-year resolution for AID events 1–7, depending on the time interval and core. The IBRD data presented here correspond to a stack of sites MD07-3133 and MD07-3134, to obtain a regional rather than local record for 20–0 ka. This stack is combined with previous data for the periods

27–7 ka[4] and 8–0 ka[24]. This new IBRD stack, the EDML1 and AICC 2012 age models and uncertainty calculations are shown in Extended Data Fig. 9. Three tables containing the IBRD data on both age scales, the age-scale tie points and the uncertainty calculations are available from the PANGAEA data server (see 'Data availability').

Comparison to cosmogenic exposure age data

In Fig. 4 and Extended Data Figs. 10, 11, we compare modelled ice-loss history in the Ross Sea and Weddell Sea regions to records of ice thinning from cosmogenic exposure age data[35] (also discussed in ref. [59]). Records at site 1 in the Ross Sea (Fig. 4) and at sites 11–15 in the Weddell Sea region (Extended Data Fig. 10) are consistent with the earlier deglaciation predicted in simulations that include a NH sea-level forcing. While exposure age data at sites 3–5 (Extended Data Fig. 11a) appear to be more consistent with a later deglaciation, these sites are just outside the region of substantial ice loss in the simulation (Extended Data Fig. 11d, e). The sites are geographically close to site S, but they exhibit substantially less thinning than the rest of the Ross Sea region (compare ice loss at red and blue squares in Extended Data Fig. 11e). On the other hand, thinning rates and timing at sites 1 and S are comparable (Extended Data Fig. 11, Fig. 4b), and more representative of regional-scale ice loss that occurs in the model during the main part of the deglaciation. Taken into consideration with the Ross Sea grounding-line record[7], it is possible that major deglaciation ends in this sector of the Ross Sea by around 8 ka, and the thinning rates observed at sites 3–5 indicate smaller-magnitude, late-Holocene ice changes. Higher-resolution ice-sheet modelling would be needed to investigate this issue further, which is infeasible in the long-timescale coupled model simulations described here.

Data availability

The datasets generated for this publication are available in the PANGAEA database (https://doi.org/10.1594/PANGAEA.919498) and as source data for Extended Data Fig. 9. The modelling results are available in the OSF database (https://osf.io/g5ur2/?view_only=8acbf1e38c184d9c8f09811c8bbef036). Source data are provided with this paper.

Code availability

The coupled ice-sheet–sea-level model used is reported in refs. [26,28]; the PSU 3D ice-sheet model is reported in ref. [37]. Ice-sheet and sea-level models are available on request from the authors of the references listed.

36. Gomez, N., Pollard, D. & Holland, D. Sea-level feedback lowers projections of future Antarctic Ice Sheet mass loss. *Nat. Commun.* **6**, 8798 (2015).
37. Pollard, D. & DeConto, R. M. Description of a hybrid ice sheet-shelf model, and application to Antarctica. *Geosci. Model Dev.* **5**, 1273–1295 (2012).
38. Kendall, R. A., Mitrovica, J. X. & Milne, G. A. On post-glacial sea level – II. Numerical formulation and comparative results on spherically symmetric models. *Geophys. J. Int.* **161**, 679–706 (2005).
39. Gomez, N., Mitrovica, J. X., Tamisiea, M. E. & Clark, P. U. A new projection of sea level change in response to collapse of marine sectors of the Antarctic Ice Sheet. *Geophys. J. Int.* **180**, 623–634 (2010).
40. MacAyeal, D. R. Large-scale ice flow over a viscous basal sediment: theory and application to ice stream B, Antarctica. *J. Geophys. Res. Solid Earth* **94**, 4071–4087 (1989).
41. Andrews, J. T. & Mahaffy, M. A. W. Growth rate of the Laurentide Ice Sheet and sea level lowering (with emphasis on the 115 000 BP sea level low). *Quat. Res.*, **6**, 167–183 (1976).
42. Pattyn, F. et al. Grounding-line migration in plan-view marine ice-sheet models: results of the ice2sea MISMIP3d intercomparison. *J. Glaciol.* **59**, 410–422 (2013).
43. Pollard, D. & DeConto, R. M. A simple inverse method for the distribution of basal sliding coefficients under ice sheets, applied to Antarctica. *Cryosphere* **6**, 953–971 (2012).
44. Pattyn, F. Sea-level response to melting of Antarctic ice shelves on multi-centennial time scales with the fast elementary thermomechanical ice sheet model (f.ETISh v1.0). *Cryosphere* **11**, 1851–1878 (2017).
45. Tsai, V. C., Stewart, A. L. & Thompson, A. F. Marine ice-sheet profiles and stability under Coulomb basal conditions. *J. Glaciol.* **61**, 205–215 (2015).
46. Le Brocq, A. M., Payne, A. J. & Vieli, A. An improved Antarctic dataset for high resolution numerical ice sheet models (ALBMAP v1). *Earth Syst. Sci. Data* **2**, 247–260 (2010).
47. Lisiecki, L. E. & Raymo, M. E. A Pliocene-Pleistocene stack of 57 globally distributed benthic $\delta^{18}O$ records. *Paleoceanography* **20**, PA1003 (2005); correction **20**, PA2007 (2005).
48. Liu, Z. et al. Transient simulation of last deglaciation with a new mechanism for Bolling-Allerod warming. *Science* **325**, 310–314 (2009).
49. Dziewonski, A. M. & Anderson, D. L. Preliminary reference Earth model. *Phys. Earth Planet. Inter.* **25**, 297–356 (1981).
50. Mitrovica, J. X. & Forte, A. M. A new inference of mantle viscosity based upon joint inversion of convection and glacial isostatic adjustment data. *Earth Planet. Sci. Lett.* **225**, 177–189 (2004).
51. Huybrechts, P. & de Wolde, J. The dynamic response of the Greenland and Antarctic ice sheets to multiple-century climatic warming. *J. Clim.* **12**, 2169–2188 (1999).
52. National Geophysical Data Center. *2-minute Gridded Global Relief Data (ETOPO2) v2* (NOAA, 2006); https://data.nodc.noaa.gov/cgi-bin/iso?id=gov.noaa.ngdc.mgg.dem:301.
53. Weber, M. E. et al. Dust transport from Patagonia to Antarctica – a new stratigraphic approach from the Scotia Sea and its implications for the last glacial cycle. *Quat. Sci. Rev.* **36**, 177–188 (2012).
54. Ruth, U. et al. "EDML1": a chronology for the EPICA deep ice core from Dronning Maud Land, Antarctica, over the last 150 000 years. *Clim. Past* **3**, 475–484 (2007).
55. Veres, D. et al. The Antarctic ice core chronology (AICC2012): an optimized multi-parameter and multi-site dating approach for the last 120 thousand years. *Clim. Past* **9**, 1733–1748 (2013).
56. Bazin, L. et al. An optimized multi-proxy, multi-site Antarctic ice and gas orbital chronology (AICC2012): 120–800 ka. *Clim. Past* **9**, 1715–1731 (2013).
57. Lamy, F. et al. Increased dust deposition in the Pacific Southern Ocean during glacial periods. *Science* **343**, 403–407 (2014).
58. Martínez-García, A. et al. Iron fertilization of the subantarctic ocean during the last ice age. *Science* **343**, 1347–1350 (2014).
59. Small, D., Bentley, M. J., Jones, R. S., Pittard, M. L. & Whitehouse, P. L. Antarctic ice sheet palaeo-thinning rates from vertical transects of cosmogenic exposure ages. *Quat. Sci. Rev.* **206**, 65–80 (2019).

Acknowledgements N.G. and H.K.H. were supported by the Natural Sciences and Engineering Research Council (NSERC), the Canada Research Chair's programme and the Canadian Foundation for Innovation, M.E.W. by the Deutsche Forschungsgemeinschaft (DFG; grant numbers We2039/8-1 and We 2039/17-1), and J.X.M. by NASA grant NNX17AE17G and Harvard University. We thank G. Tseng for assistance with exploratory research that informed this study, and D. Pollard for insight on and use of the PSU ice-sheet model.

Author contributions N.G. contributed the numerical modelling and analysis; H.K.H. prepared model input; M.E.W. contributed iceberg-rafted debris records and, together with P.U.C. and J.X.M., other published data and related discussion. All authors contributed to developing the idea and to writing and refining the manuscript.

Competing interests The authors declare no competing interests.

Additional information

Correspondence and requests for materials should be addressed to N.G.

Peer review information *Nature* thanks Frank Pattyn and the other, anonymous, reviewer(s) for their contribution to the peer review of this work.

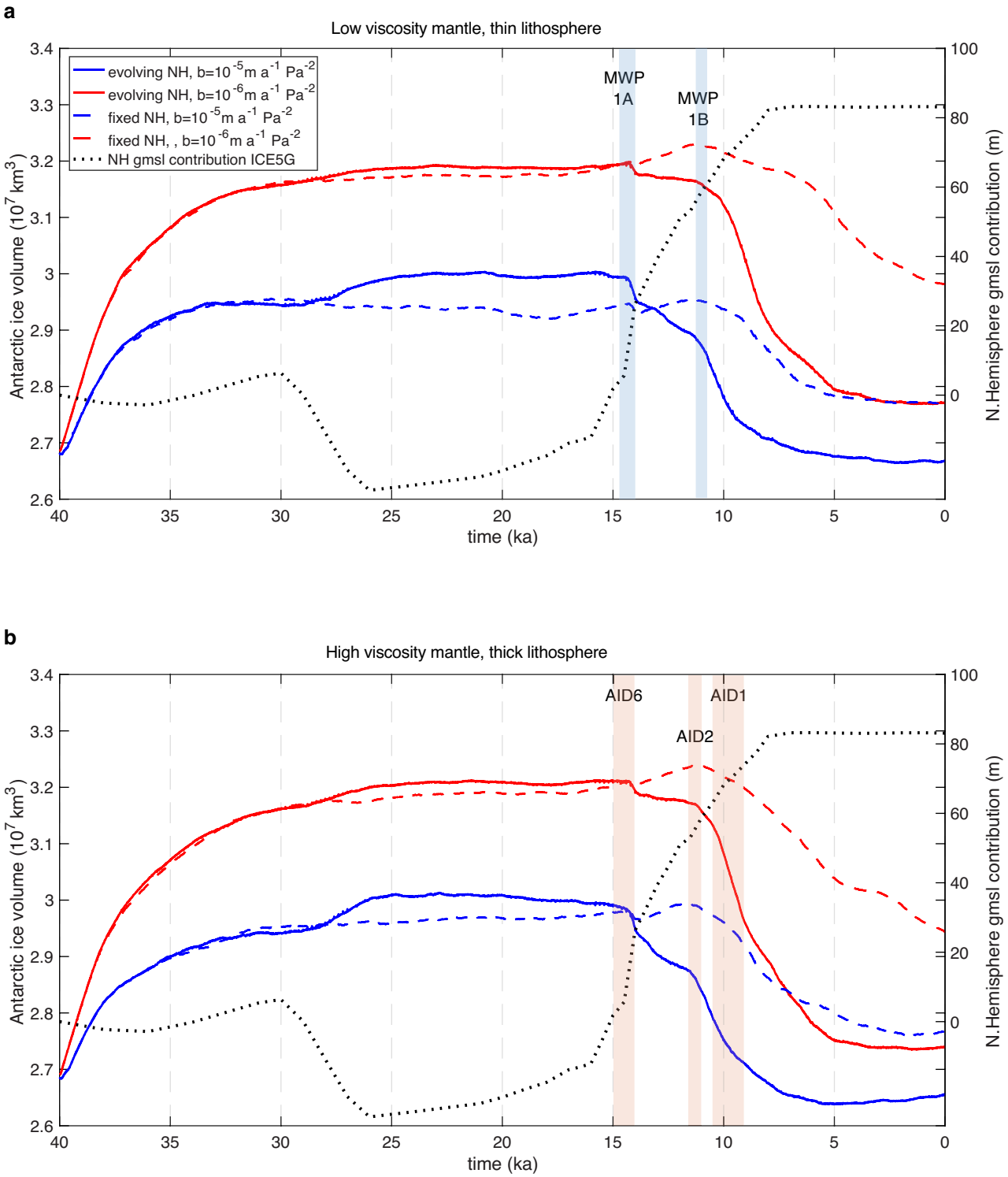

Extended Data Fig. 1 | Sensitivity of results to ice and Earth model parameters. a, Changes in Antarctic ice volume predicted in simulations with evolving (solid lines) and fixed (dashed lines) Northern Hemisphere ice mass, and adopting the LVZ Earth model (Methods). Blue lines are identical to those in Fig. 2b, corresponding to a basal sliding coefficient of $b = 10^{-5}$ m yr^{-1} Pa^{-2}; red lines correspond to a basal sliding coefficient of $b = 10^{-6}$ m yr^{-1} Pa^{-2}. The black dotted line shows changes in Northern Hemisphere ice volume (right axis; in metres of global-mean sea level (gmsl) equivalent) prescribed in the ICE5G[27] ice history. **b**, As in **a**, but adopting the HV Earth model (Methods). Blue (**a**) and red (**b**) vertical bands represent the timing of MWP and AID events, as in Fig. 2a, c, respectively.

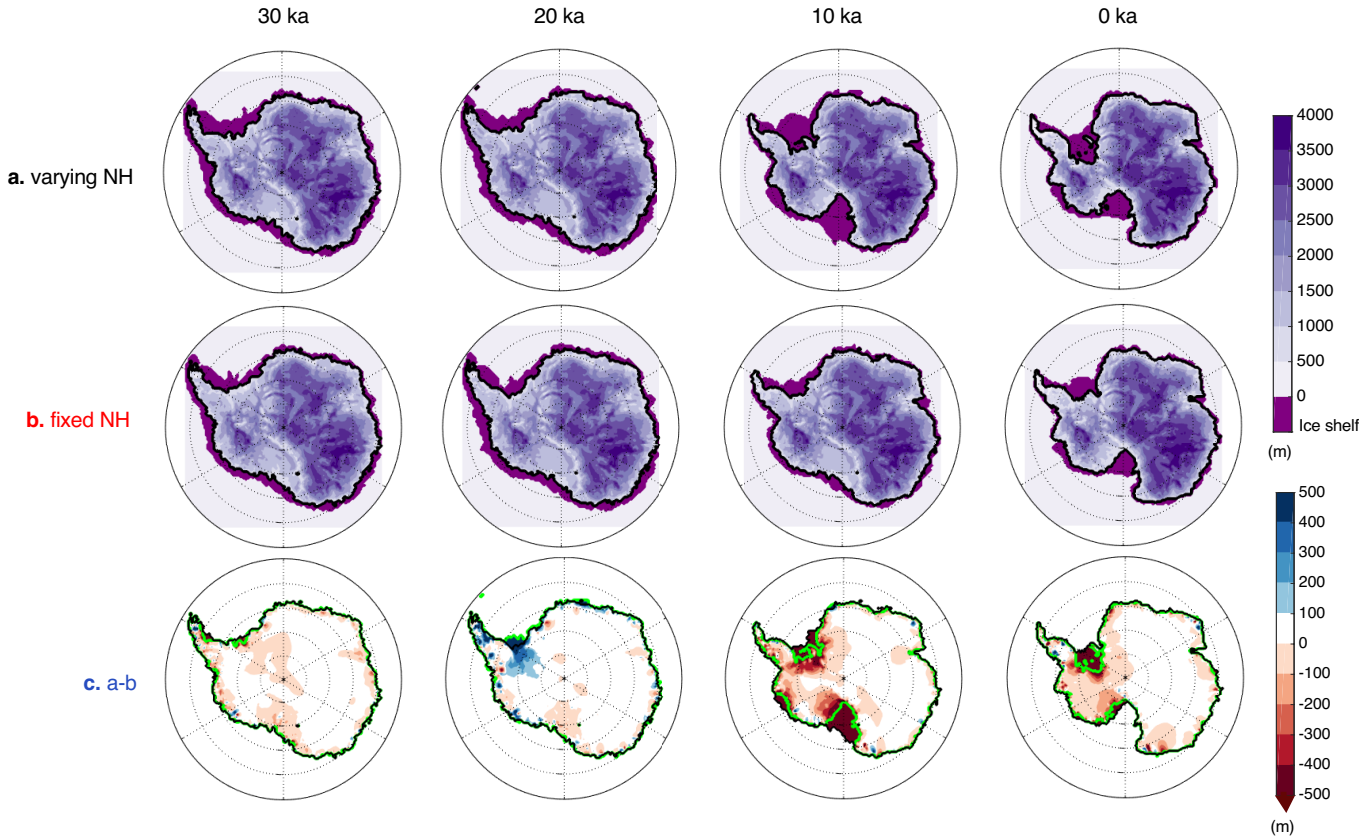

Extended Data Fig. 2 | Evolution of Antarctic ice cover with and without Northern Hemisphere sea-level forcing. a, **b**, Thickness of grounded ice (in metres) and extent of ice shelves, at 30 ka, 20 ka, 10 ka and the present day, predicted from simulations that include variations in the Northern Hemisphere ice sheets represented by the ICE5G[27] ice history (**a**) and from simulations in which ice cover in the Northern Hemisphere remains fixed (**b**). Black lines show the grounding lines. **c**, The difference in grounded ice thickness between simulations in **a** and **b**, representing the effect of sea-level changes associated with Northern Hemisphere ice sheets on the evolution of the AIS. Green and black lines represent the positions of the grounding lines with (**a**) and without (**b**) the Northern Hemisphere sea-level forcing included.

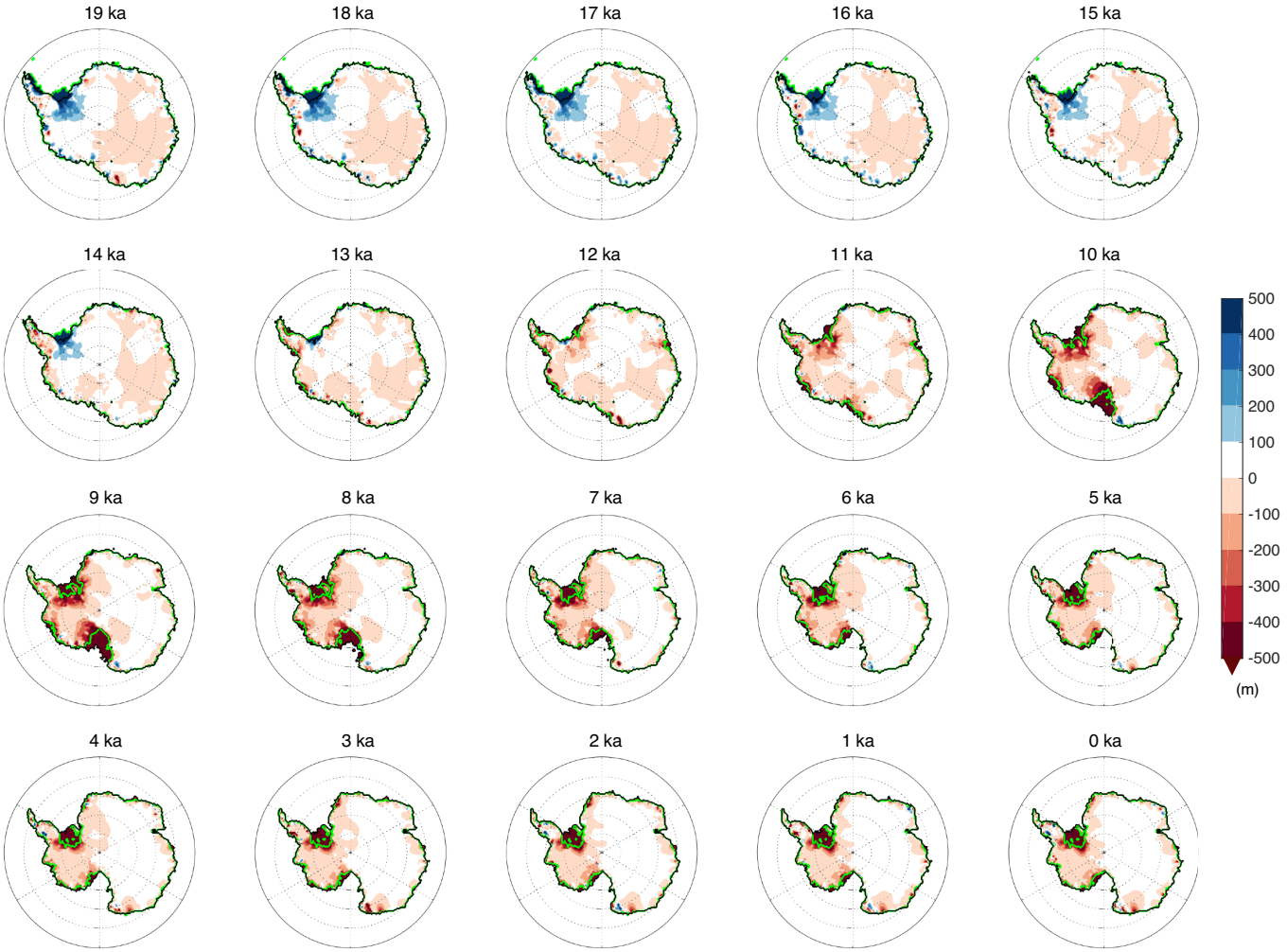

Extended Data Fig. 3 | Influence of Northern Hemisphere sea-level forcing on Antarctic ice cover during the deglaciation. The colour scale indicates the difference in the thickness (in metres) of grounded ice, at the indicated times, between simulations that include variations in the Northern Hemisphere ice sheets from ICE5G[27] ice history and in which ice cover in the Northern Hemisphere remains fixed throughout the simulation. Differences are displayed as in Fig. 3c, but every 1 kyr for the past 19 kyr. Green and black lines represent the positions of the grounding lines with and without the Northern Hemisphere sea-level forcing included, respectively.

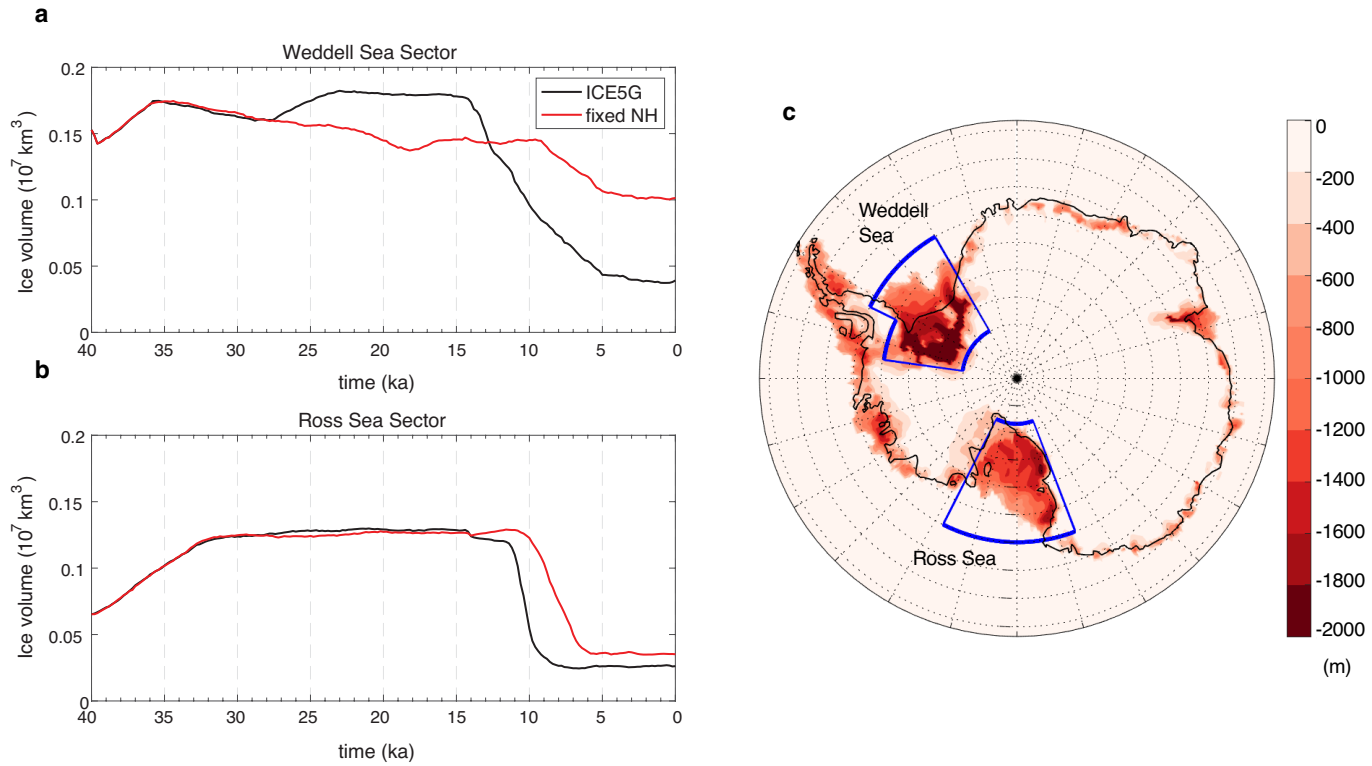

Extended Data Fig. 4 | Antarctic ice-volume changes in the Ross Sea and Weddell Sea sectors. a, Changes in ice volume in the Weddell Sea sector predicted in simulations with fixed (red) and evolving (black) Northern Hemisphere ice from the ICE5G[27] ice history. **b**, As in **a**, but for the Ross Sea sector. **c**, Blue lines outline the areas included in the calculations in **a** and **b**; colour scale indicates the change in ice thickness (in metres) from 20 ka to the present day in the simulations that include Northern Hemisphere ice-cover changes from ICE5G[27].

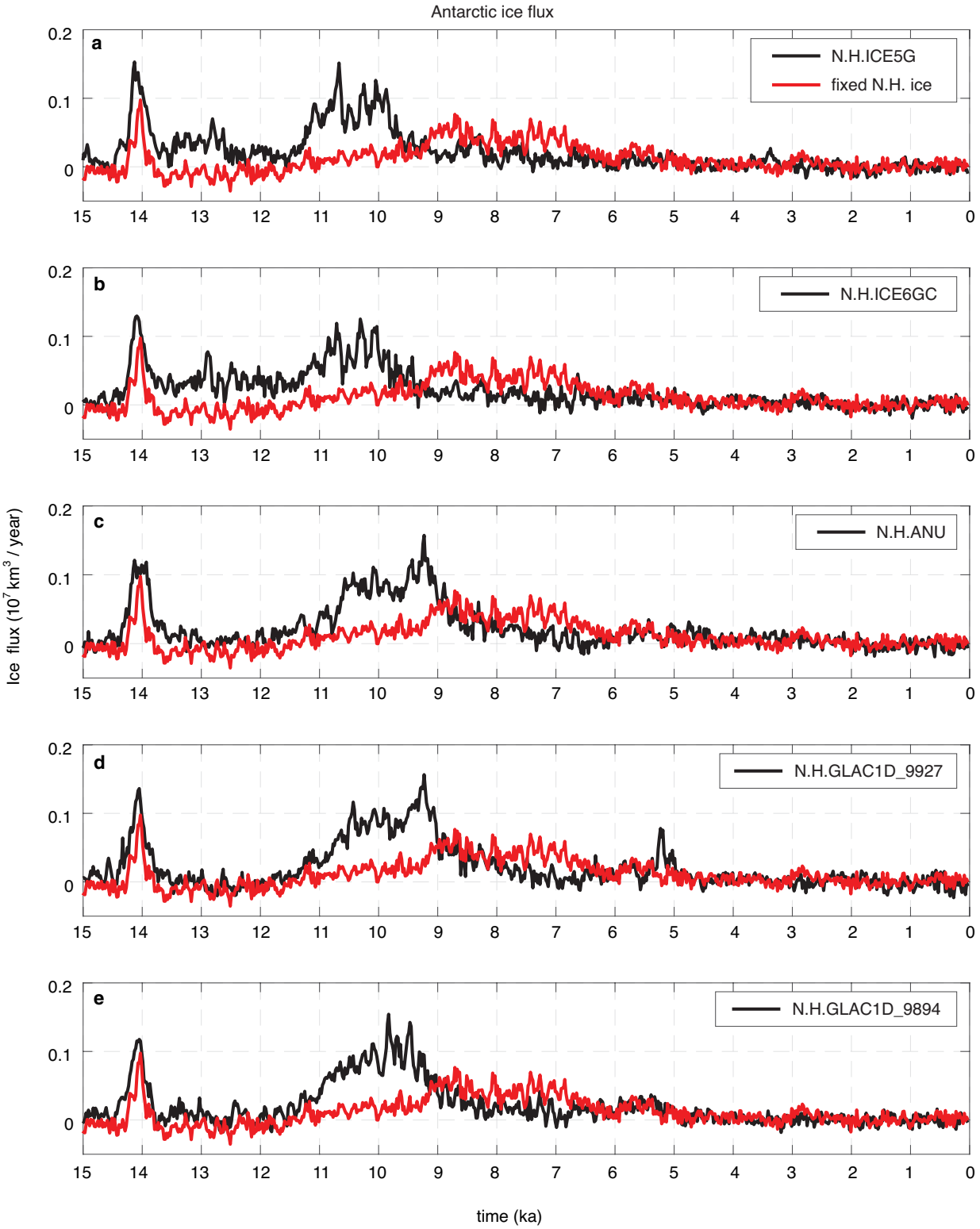

Extended Data Fig. 5 | Influence of Northern Hemisphere sea-level forcing on the rate of Antarctic ice loss. a–**e**, Rate of change of Antarctic ice volume, including grounded and floating ice, calculated with a 100-year running mean, predicted from simulations including (black) and excluding (red) Northern Hemisphere ice-cover changes, using the ice histories indicated in the legend (Methods). The mean and standard deviation of these five panels are shown in Fig. 3a.

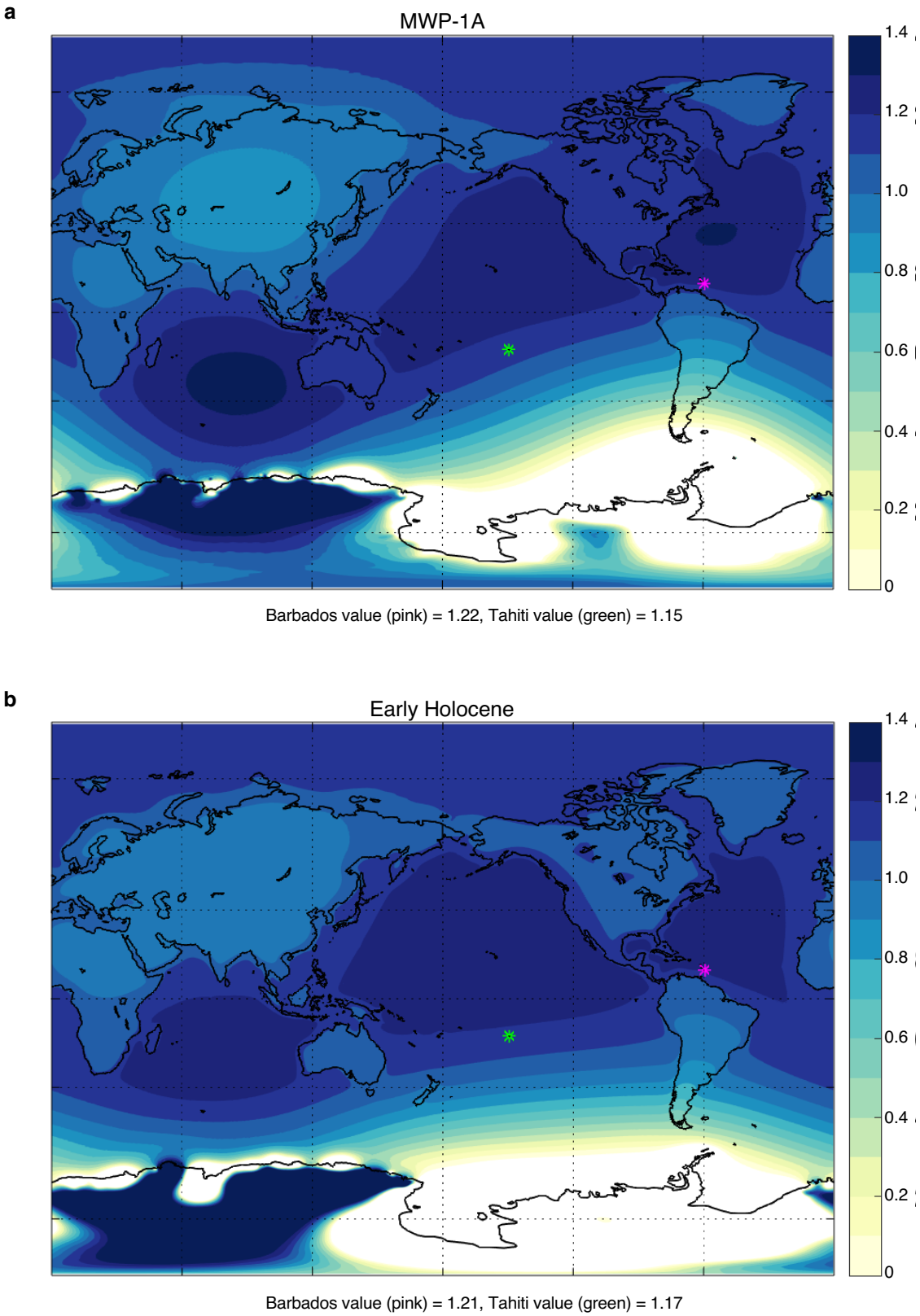

Extended Data Fig. 6 | Patterns of sea-level change for Antarctic ice loss during MWP-1A and the early Holocene. a, **b**, Predicted sea-level change, normalized by the global-mean sea-level-equivalent associated with Antarctic ice loss during MWP-1A (**a**) and the early Holocene (including MWP-1B; **b**). Calculations are associated with simulations that include Northern Hemisphere ice cover changes given by ICE5G[27]. The patterns of sea-level change and the global mean sea-level equivalent used in the normalization are calculated over the time windows indicated by the green vertical bands in Fig. 2b. Green and magenta asterisks indicate the locations of the far-field relative sea-level records in Tahiti and Barbados.

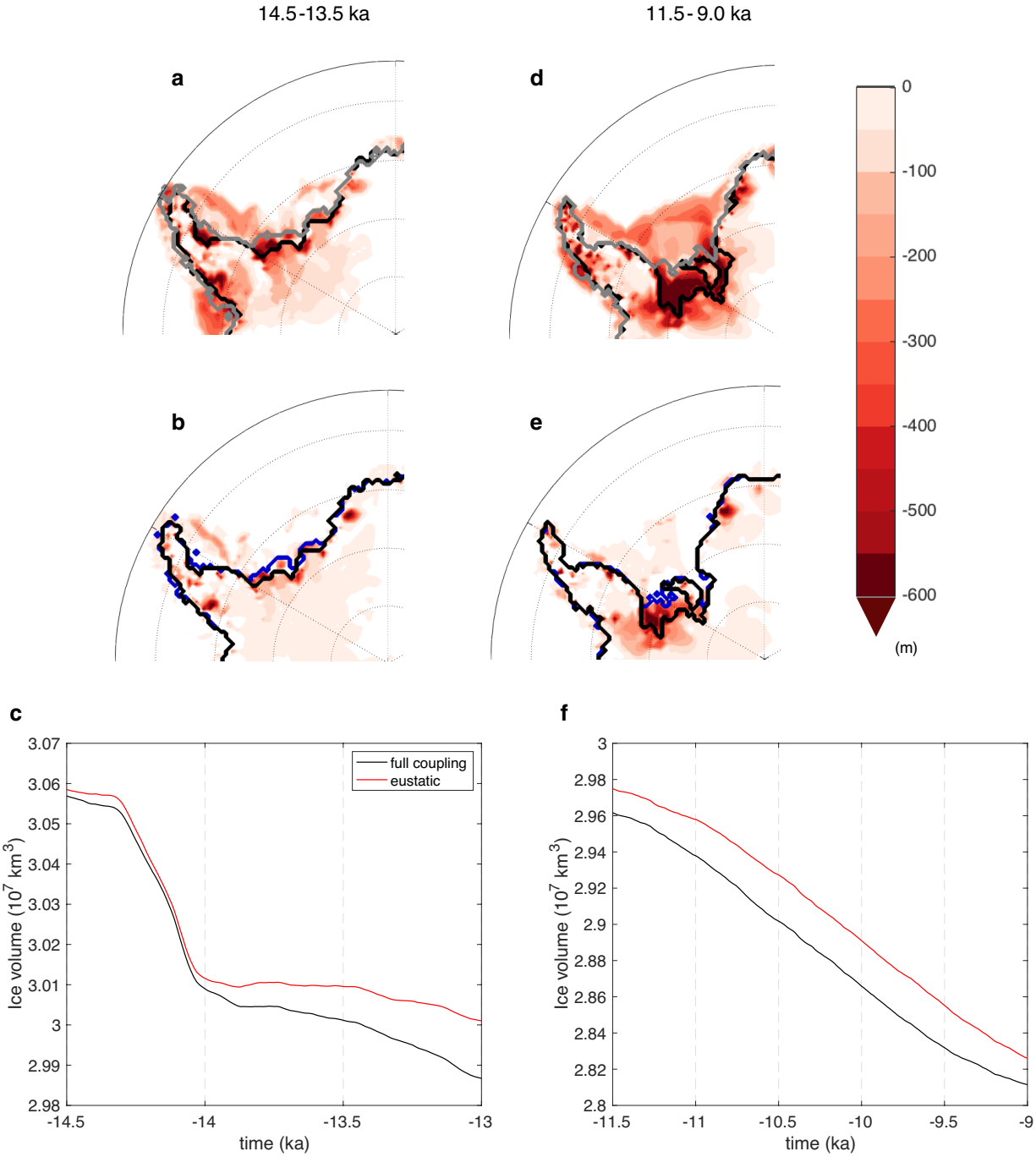

Extended Data Fig. 7 | Sensitivity of the Weddell Sea sector to geographic variability in sea-level forcing. a, Same as Fig. 3b, but zoomed in on the Weddell Sea region, where geographically variable sea-level changes associated with Northern Hemisphere ice loss are largest (Fig. 1c). The colour scale shows the change in ice thickness predicted from a simulation adopting the ICE5G[27] ice history in the Northern Hemisphere, which includes geographically variable sea-level changes associated with gravitational, deformational and Earth rotational effects activated by ice-cover changes globally, during MWP-1A (14.5–13.5 ka). Grey and black lines indicate the grounding-line position at the start and end of the time interval, respectively. **b**, The difference between **a** and the same calculation but adopting the simulation with globally uniform sea-level change from the Northern Hemisphere. The black line is as in **a**; the blue line indicates the grounding-line position at the end of the time interval for the uniform sea-level simulation. **c**, Antarctic ice-volume variations from simulations with geographically variable (black) and uniform (red) sea-level changes associated with Northern Hemisphere ice loss over the MWP-1A interval. **d**–**f**, As in **a**–**c**, but for the early Holocene interval (11.5–9 ka). In this case, **d** is the same as Fig. 3d, but zoomed in on the Weddell Sea region. The uniform sea-level change is calculated relative to modern topography and scaled such that the total contribution to global sea-level change from the Northern Hemisphere over the last deglaciation (since 21 ka) is 95.5 m, in agreement with ref. [27].

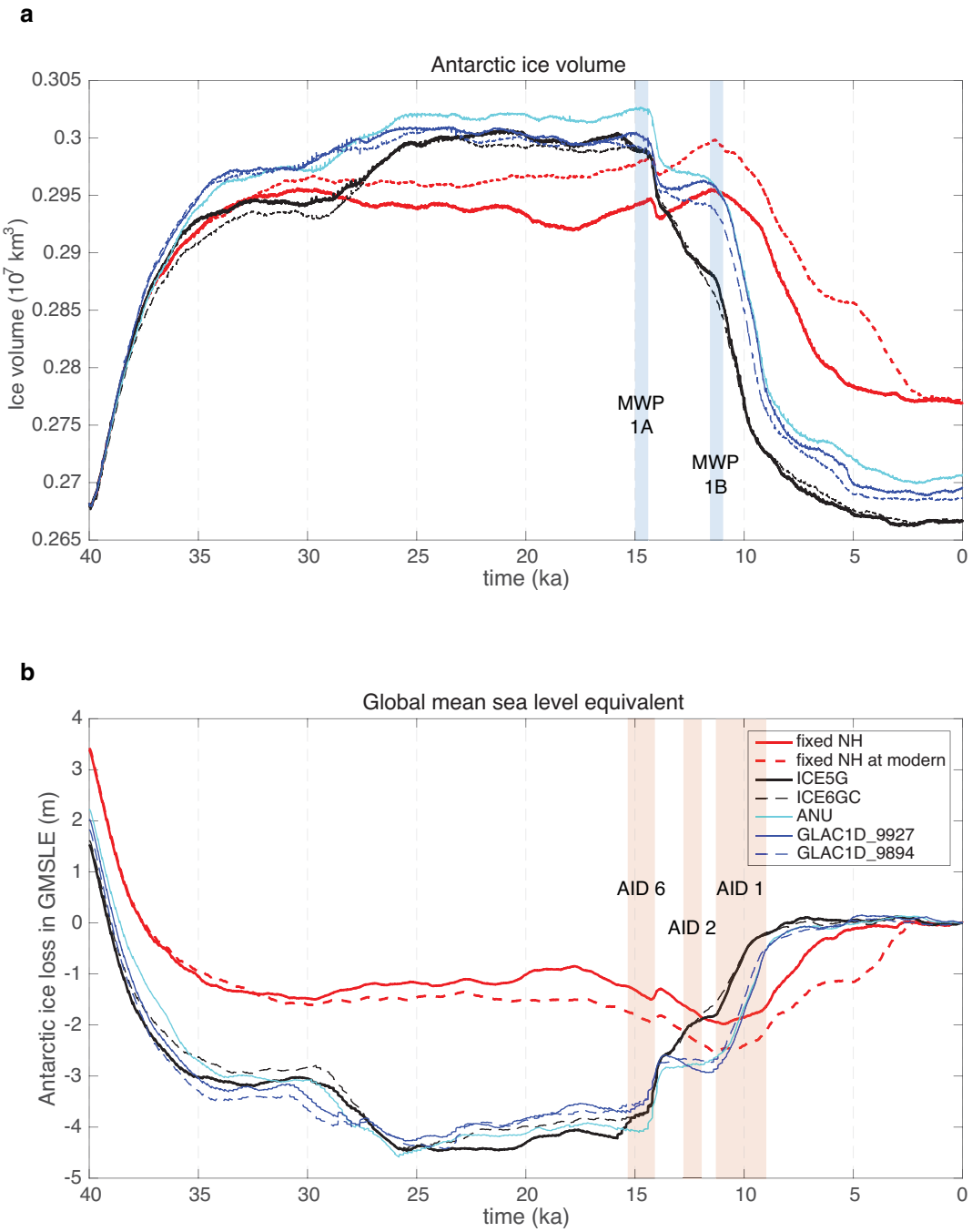

Extended Data Fig. 8 | Predicted Antarctic ice-volume changes and global-mean sea-level contributions. a, Changes in AIS volume predicted in a simulation with Northern Hemisphere ice cover fixed at the 40 ka configuration within ICE5G[27] (solid red line) and in simulations with evolving Northern Hemisphere ice adopting the ICE5G[27] (solid black line), ICE6GC[31] (dashed black line) and ANU[30] (cyan line) ice histories, as well as two composite ice histories in which ice cover over North America and Greenland in ICE5G has been replaced by regional GLAC1D[29] models (blue lines). The dashed red line represents a simulation in which the Northern Hemisphere ice sheets are fixed at the modern configuration rather than at the 40 ka configuration throughout the simulation. In this case, marine-based sectors of the AIS start on even shallower bedrock, and hence the predicted ice-sheet growth is larger at the LGM, while the ice loss during the deglaciation occurs later and is of even smaller magnitude than in the original simulation. Note that this is not a realistic starting configuration. **b**, As in **a**, but expressed as a global-mean sea-level-equivalent (GMSLE) relative to the modern state. This is calculated by taking the ice above floatation thickness in Antarctica relative to the palaeo bedrock topography at each time step in the model, and dividing by the area of the modern ocean. Note that **a** and **b** are not directly proportional because as the bedrock topography in Antarctica evolves the volume of ice above floatation in marine sectors also changes. Blue (**a**) and red (**b**) vertical bands represent the timing of MWP and AID events, as in Fig. 2a, c, respectively.

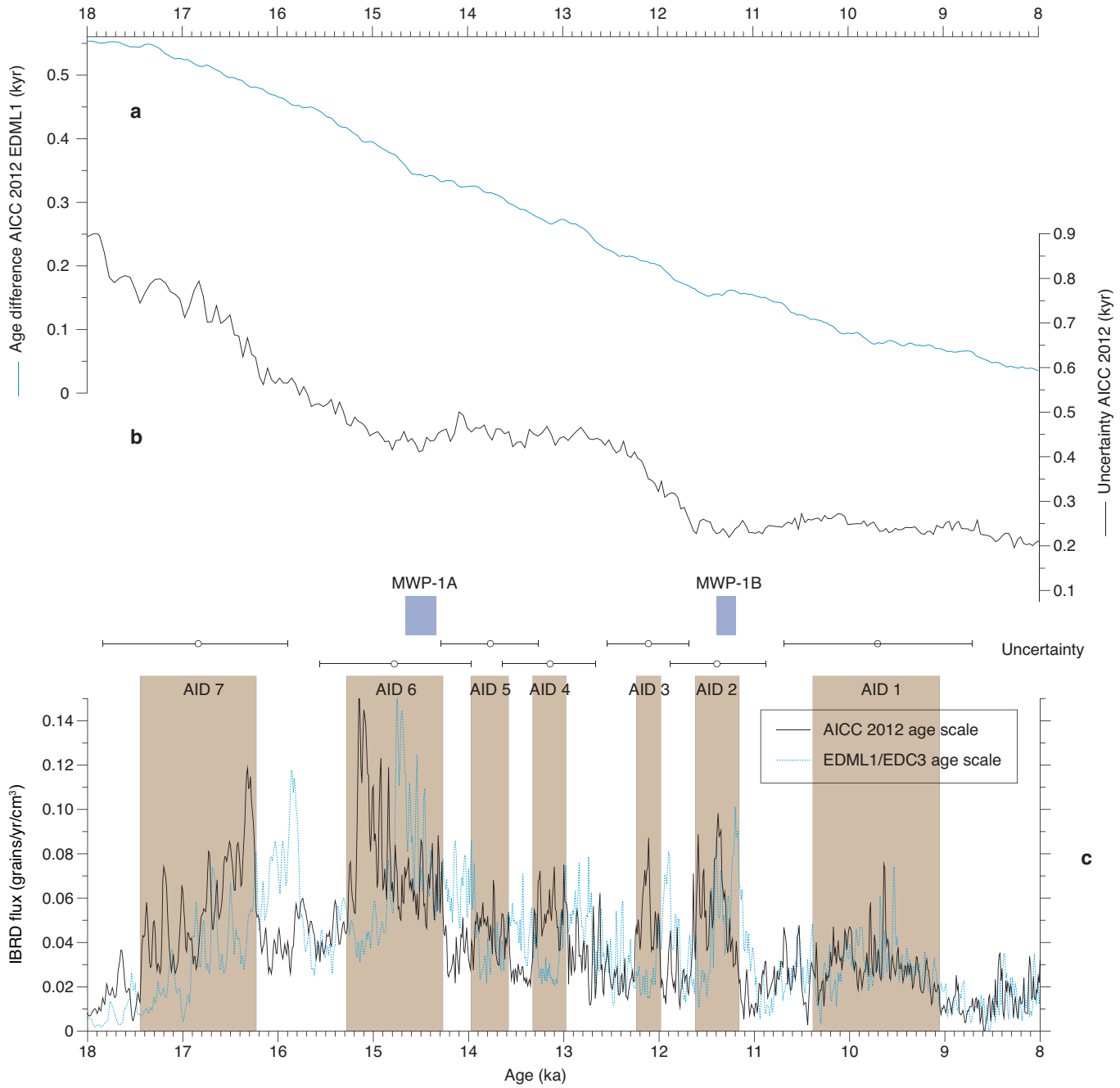

Extended Data Fig. 9 | Age model comparison and uncertainty for IBRD flux record from Iceberg Alley. a, Age difference between the AICC 2012[55,56] and EDML1[54] age models. **b**, Age uncertainty in the AICC 2012 age model. **c**, IBRD flux time series adopting the AICC 2012 (black line, as in Figs. 2c, 4b) and EDML1/EDC3 (blue dotted line) age scales. The IBRD stack is composed of records from sites MD07-3133 and MD07-3134. It is presented here for 20–0 ka and was combined with previous data for 27–7 ka[4] and 8–0 ka[24]. Vertical brown bars indicate AID events 1–7[4] on the AICC 2012 age scale. Blue vertical bars indicate MWP-1A[21] and MWP-1B[22]. Horizontal black error bars show propagated uncertainties for the upper and lower bounds of each AID event for errors in tie-point correlation to EDML[4] and uncertainties of the AICC 2012 age model..

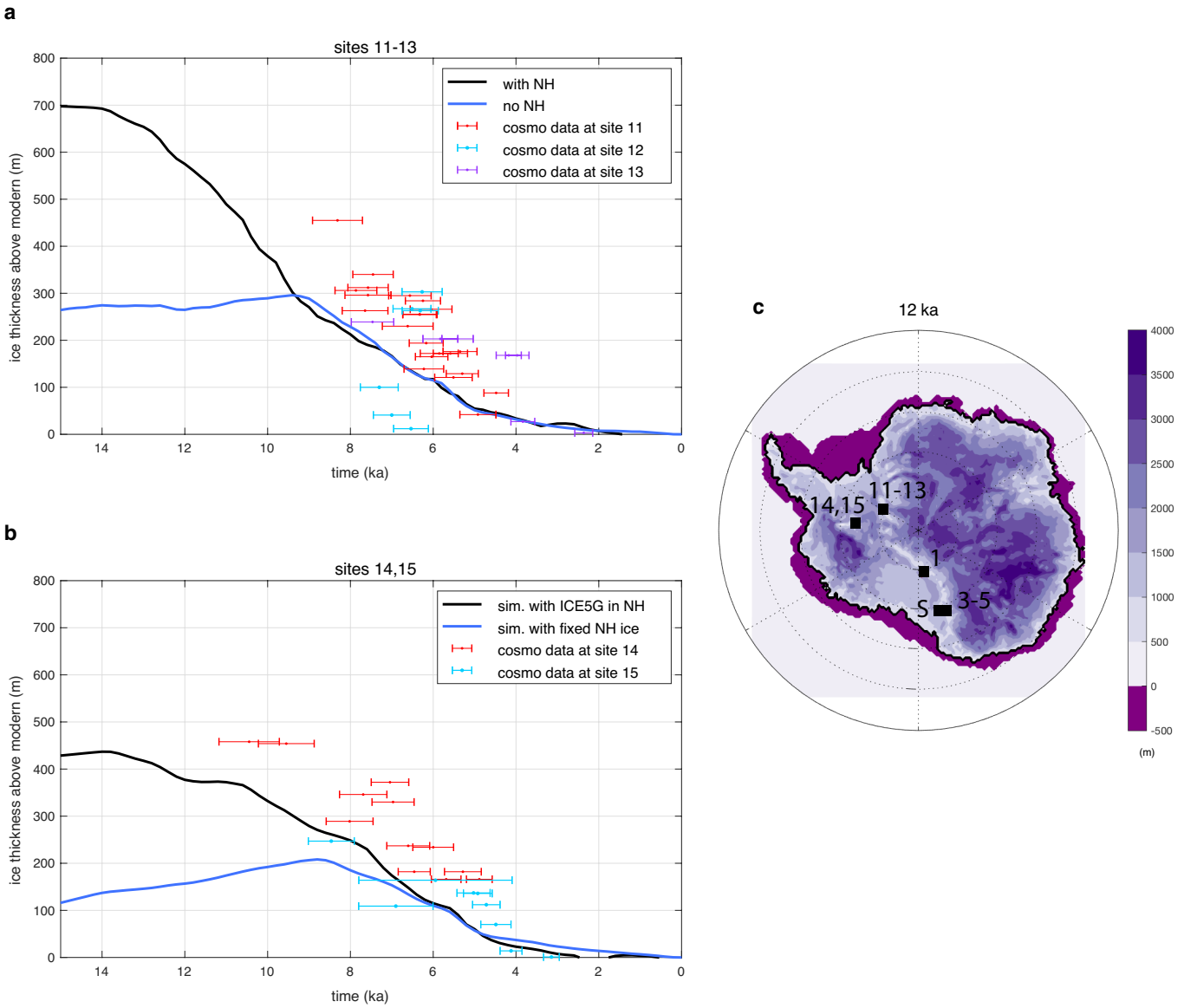

Extended Data Fig. 10 | Comparison of predicted and observed ice-thickness changes in the Weddell Sea region. a, **b**, Predicted (lines) and observed (error bars) ice thickness (in metres) above the modern thickness at sites 11–13 (**a**) and 14, 15 (**b**) from ref. [35]. Predictions are from simulations in which Northern Hemisphere ice cover is evolving according to ICE5G[27] (black lines) or is fixed (blue lines). Error bars show cosmogenic exposure age data with 2σ uncertainty from ref. [35]. **c**, Map of predicted ice thickness at 12 ka, in the simulation with ICE5G[27]. The locations of the relevant sites in the Weddell Sea and Ross Sea (see Extended Data Fig. 11) regions are indicated. See Methods for further discussion of these results.

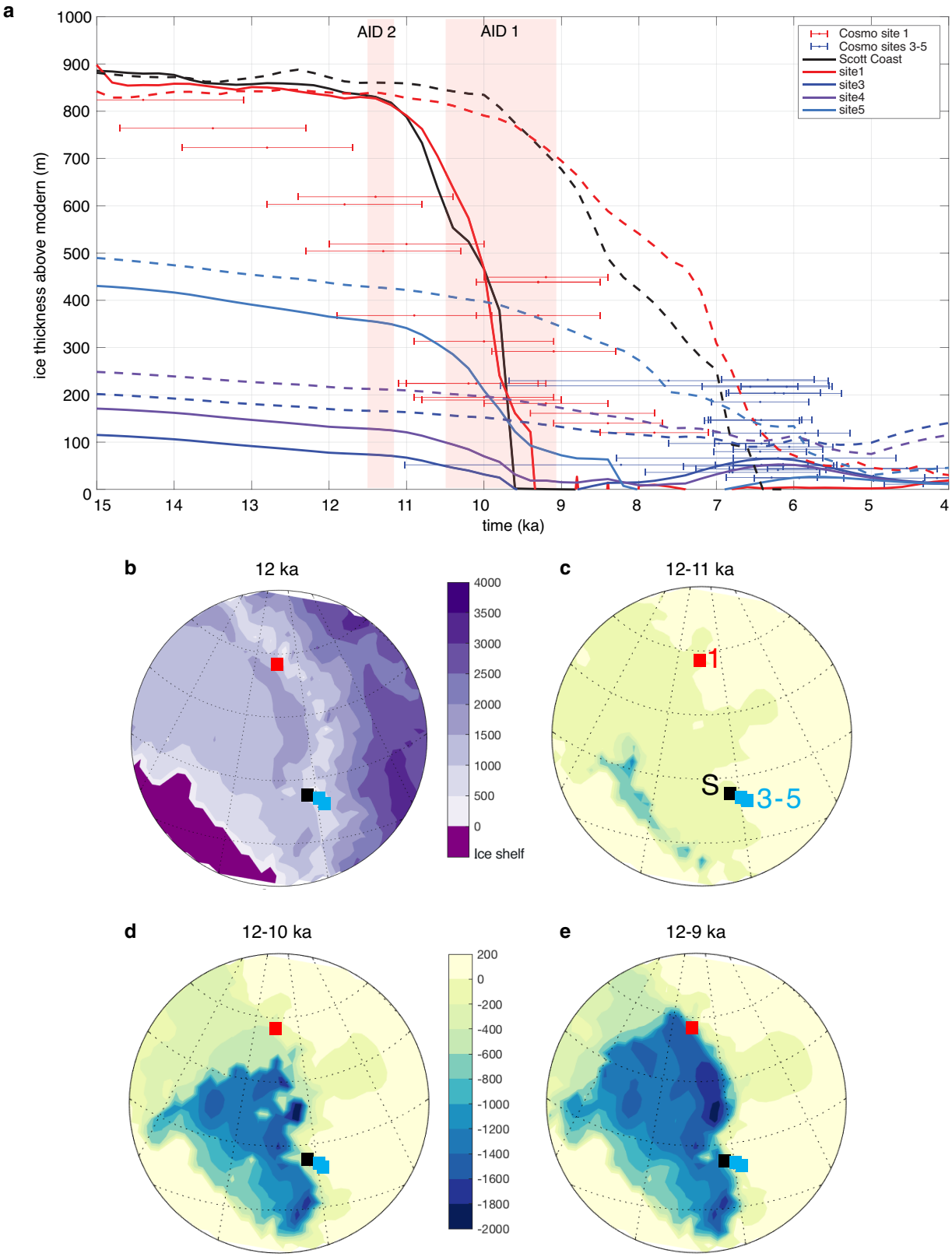

Extended Data Fig. 11 | Comparison of predicted and observed ice-thickness changes in the Ross Sea region. a, Predicted (lines) and observed (2σ error bars) ice thickness (in metres) above the modern thickness at Scott Coast site S (black) and sites 1 (red) and 3–5 (shades of blue) from ref. [35]. The locations of the sites are indicated in **b**–**e**. Predictions are from simulations in which Northern Hemisphere ice cover is evolving according to ICE5G[27] (solid lines) or is fixed (dashed lines). Observations are cosmogenic exposure age data from ref. [35]. Red vertical bands represent the timing of AID events 1 and 2, as in Fig. 2c. **b**, Map of predicted ice thickness 12 ka in the Ross Sea, in the simulation with evolving Northern Hemisphere ice. **c**–**e**, The difference in ice thickness between 12 ka (**b**) and 11 ka (**c**), 10 ka (**d**) and 9 ka (**e**). See Methods for further discussion of these results.